

A Single- to Few-Layer Nanoparticle Cathode Coating for Thiophosphate-Based All-Solid-State Batteries

Yuan Ma,^{[a] ‡} Ruizhuo Zhang,^{[a] ‡} Yushu Tang,^{[b] *} Yanjiao Ma,^[b] Jun Hao Teo,^[a] Thomas Diemant,^[c] Damian Goonetilleke,^[a] Jürgen Janek,^[a,d] Matteo Bianchini,^[a,e] Aleksandr Kondrakov,^[a,e] and Torsten Brezesinski^{[a] *}*

[a] Battery and Electrochemistry Laboratory, [b] Institute of Nanotechnology, Karlsruhe Institute of Technology (KIT), Hermann-von-Helmholtz-Platz 1, 76344 Eggenstein-Leopoldshafen, Germany

[c] Helmholtz Institute Ulm (HIU) for Electrochemical Energy Storage, Helmholtzstr. 11, 89081 Ulm, Germany

[d] Institute of Physical Chemistry & Center for Materials Research (ZfM/LaMa), Justus-Liebig-University Giessen, Heinrich-Buff-Ring 17, 35392 Giessen, Germany

[e] BASF SE, Carl-Bosch-Str. 38, 67056 Ludwigshafen, Germany

ABSTRACT

Bulk-type solid-state batteries (SSBs) composed of lithium thiophosphate superionic solid electrolytes (SEs) and high-capacity cathode active materials (CAMs) have recently attracted much attention for their potential application in next-generation electrochemical energy storage. However, compatibility issues between the key components in this kind of battery system are difficult to overcome. Here we report on a protective cathode coating that strongly reduces the prevalence of detrimental side reactions between CAM and SE during battery operation. This is demonstrated using preformed HfO₂ nanoparticles as a secondary particle coating for a layered Ni-rich oxide CAM, LiNi_{0.85}Co_{0.1}Mn_{0.05}O₂ (NCM85). Preparation of a stable dispersion of the HfO₂ nanoparticles enabled the deposition of a uniform coating of thickness ≤ 11 nm. When incorporated into Li₆PS₅Cl-based, pellet-stack SSBs, the coated NCM85 showed superior performance in terms of reversibility, cell capacity, longevity, and rate capability over

its uncoated counterpart. The effectiveness of the protective coating in mitigating electro-chemo-mechanical degradation was investigated using a suite of physical and electrochemical characterization techniques. In addition, the adaptability to wet processing of the coated NCM85 is demonstrated in slurry-cast SSBs and liquid electrolyte-based Li-ion cells.

KEYWORDS

solid-state battery, secondary particle coating, Ni-rich cathode, argyrodite solid electrolyte, electro-chemo-mechanical degradation

INTRODUCTION

Solid-state batteries (SSBs) have been investigated intensively as a promising next-generation energy-storage technology in recent years.^{1,2} The adoption of inorganic solid electrolytes (SEs) in these systems can enhance safety, due to the replacement of flammable (organic) liquid electrolytes in conventional lithium-ion batteries (LIBs).²⁻⁴ More importantly, the use of SEs can facilitate the implementation of Li metal or alloy anodes, ultimately leading to improvements in cell-level energy density (thanks to their large Li transference number and increased mechanical rigidity).^{1,3,5,6} For example, lithium thiophosphate superionic SEs (e.g. $\text{Li}_6\text{PS}_5\text{Cl}$ with $\sigma_{\text{ion}} \approx 3 \times 10^{-3}$ S/cm at room temperature) have been thoroughly examined recently, with the goal of ensuring satisfactory rate capability of the respective SSBs, among others.^{2,7,8} However, the main drawback of sulfide SEs is their narrow electrochemical stability window.^{2,7-9} When using industrially relevant cathode active materials (CAMs), such as $\text{LiNi}_{0.85}\text{Co}_{0.1}\text{Mn}_{0.05}\text{O}_2$ (NCM851005, hereafter referred to as NCM85), the poor stability at the CAM/SE interface induces side reactions, resulting in resistance buildup and inferior electrochemical performance.^{2,8-11}

To address interfacial stability problems, numerous studies have proposed the application of a protective coating to the CAM surface to prevent direct physical contact with the SE.^{2,9,12,13} In principle, a coating should have the following characteristics: (i) nanoscale thickness, (ii) structural/morphological uniformity, (iii) high (electro)chemical stability, and (iv) reasonable ionic conductivity.^{2,10,13} However, the available coating methods, especially wet-chemical (sol-

gel) techniques, have some limitations for the preparation of conformal surface films on complex substrates (regarding uniformity/degree of coverage, coating chemistry, etc.).^{10,14–18} Despite progress made with physical deposition techniques, their widespread application has been hampered by difficulties in the scalability and high production costs, caused by complex processes.^{19,20}

In this work, we present an optimized wet-chemistry route to apply nanoparticles (NPs) dispersed in solution as coating material.⁸ Different from previous NP-derived coatings, surface stabilization effectively solved problems associated with particle agglomeration, thus practically realizing the deposition of single NPs (**Figure 1a**).^{8,21–23} The effectiveness of NP coatings, in general, was studied by using HfO₂-coated NCM85 (HfO₂-NCM85) as a model-type CAM in Li₆PS₅Cl-based SSB cells with an Li₄Ti₅O₁₂ (LTO) anode. Note that HfO₂ has already been demonstrated to be an (electro)chemically stable coating material.²⁰ Electrochemical testing of the CAM in LIBs and slurry-cast SSBs also highlights the practicality of the NP coating for wet-processing techniques. The combination of both physical and electrochemical characterization techniques offered insights into the working principle of the protective coating, which helped to understand differences in cyclability between the bare and coated NCM85 samples.

RESULTS AND DISCUSSION

The HfO₂ NPs were prepared using a surfactant-free solvothermal process (characterization results can be found in the Supporting Information, see **Figures S1** and **S2**).^{8,24,25} After synthesis, a white suspension (**Figure S1a**) was obtained, indicative of particle agglomeration (by virtue of their high surface energy).^{26,27} It should be noted that NPs present in such an agglomerated state are not well suited for coating applications.^{8,27} To this end, we also found that redispersing them in apolar or polar solvents does not lead to any improvements. Surface modification was thus performed to increase their dispersibility. A quasi-transparent dispersion in chloroform (**Figure S1b**) was achieved by adding small amounts of oleic acid and oleylamine, offering stabilization owing to steric hindrance.²⁴ Transmission electron microscopy (TEM) images taken after surface treatment (**Figures S1c-e**) showed elongated (crystalline) NPs of size 6-7

nm (**Figures S1f and g**) that were virtually free of agglomeration.

HfO₂-NCM85 was produced via a typical wet-chemistry coating route, by combining the NPs dispersed in chloroform with bare CAM and subsequent heating at 400 °C in O₂. The Hf content from inductively coupled plasma-optical emission spectroscopy (ICP-OES, **Table S1**) was found to be 0.72 wt. % (0.83 wt. % HfO₂). It should be noted that both the heating temperature and coating content were optimized based on a series of experiments. After the coating process, the CAM was found to retain the expected layered structure with space group *R-3m*. X-ray diffraction (XRD) and Rietveld refinement profiles and refined structural parameters are shown in **Figure 1b** and **Table S2**, respectively. Compared to the uncoated reference material (**Figure S3**), a subtle increase in cell volume was observed after coating, by $\sim 0.1 \text{ \AA}^3$, while the degree of Ni²⁺/Li⁺ cation mixing remained similar for both samples, 3.9(3) and 3.4(2) % for bare NCM85 and HfO₂-NCM85, respectively. This demonstrates that the coating process is not detrimental to the structural properties of the CAM.²⁸ No reflections from the HfO₂ NPs were apparent in the XRD pattern (zoom presented in **Figure S4**), which could be expected given the low weight content of the coating.

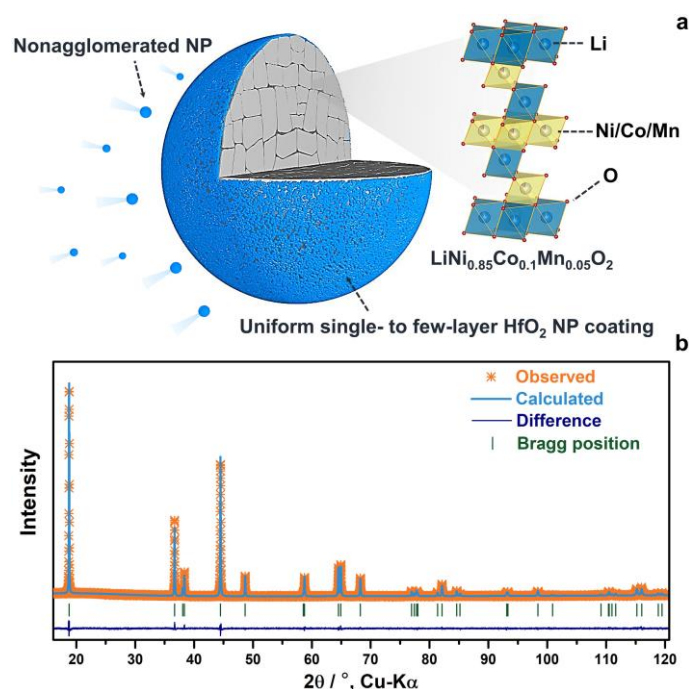


Figure 1. (a) Schematic depiction of the bulk and surface (coating) structure for HfO₂-NCM85. (b) XRD pattern collected from the HfO₂-NCM85 particles and corresponding Rietveld refinement plot. Observed, calculated, and difference profiles are shown in orange, cyan, and

blue, respectively. Green markers indicate the expected Bragg reflections for NCM85. Refinement results are shown in **Table S2**.

To gain more insight into the structural characteristics of the NCM85 prior to and after coating, scanning electron microscopy (SEM), high-angle annular dark-field (HAADF) scanning TEM (STEM), and X-ray photoelectron spectroscopy (XPS) measurements were conducted on the samples. As can be seen from the high- and low-magnification SEM images in **Figures 2a** and **b** (lower magnification images are shown in **Figure S5**), unlike bare NCM85, the HfO₂-NCM85 CAM exhibits a rougher surface structure, without visible NP agglomeration at this scale, but the particle morphology is well maintained. Results from (S)TEM analysis and energy-dispersive X-ray spectroscopy (EDS) mapping of focused ion beam (FIB)-prepared specimens are presented in **Figures 2c-f**. The HAADF STEM image in **Figure 2c** shows the presence of a uniform shell-like structure on the surface of HfO₂-NCM85. The coating thickness is around 11 nm. TEM imaging unveiled that the surface shell can be described as a single- to few-layer nanoparticle coating (**Figures 2d, e** and **S6**). In agreement with the (S)TEM results, EDS mapping (**Figure 2f**) confirmed that the HfO₂ NPs are primarily located on the free (outer) surface of the NCM85 secondary particles. Compared with previous reports on NP coatings, significant improvements regarding uniformity and thickness were achieved in this work (**Table S3**).

The surface composition was probed by XPS (**Figures 2g-j**). As expected, Hf 4d signals were detected only for HfO₂-NCM85 (**Figure 2g**). Their binding energies (213.2/224.8 eV) are characteristic of Hf⁴⁺.^{29,30} The detail spectrum of the C 1s region for bare NCM85 revealed three peaks (**Figure 2h**), which can be assigned to C=C/C-C (284.8 eV), C-O (286.8 eV), and O=C-O (288.8 eV) species.³¹⁻³³ Interestingly, the intensity of the carbonaceous signals did not change much with coating, suggesting that the surface ligands are decomposed during the final heat treatment. The Ni 2p and Co 2p detail spectra of HfO₂-NCM85 showed much decreased peak intensities over the bare NCM85 (**Figures 2i** and **j**). Considering the surface sensitivity of XPS, the weaker signals indicate a high degree of surface coverage by the HfO₂ nanoparticles.²⁸

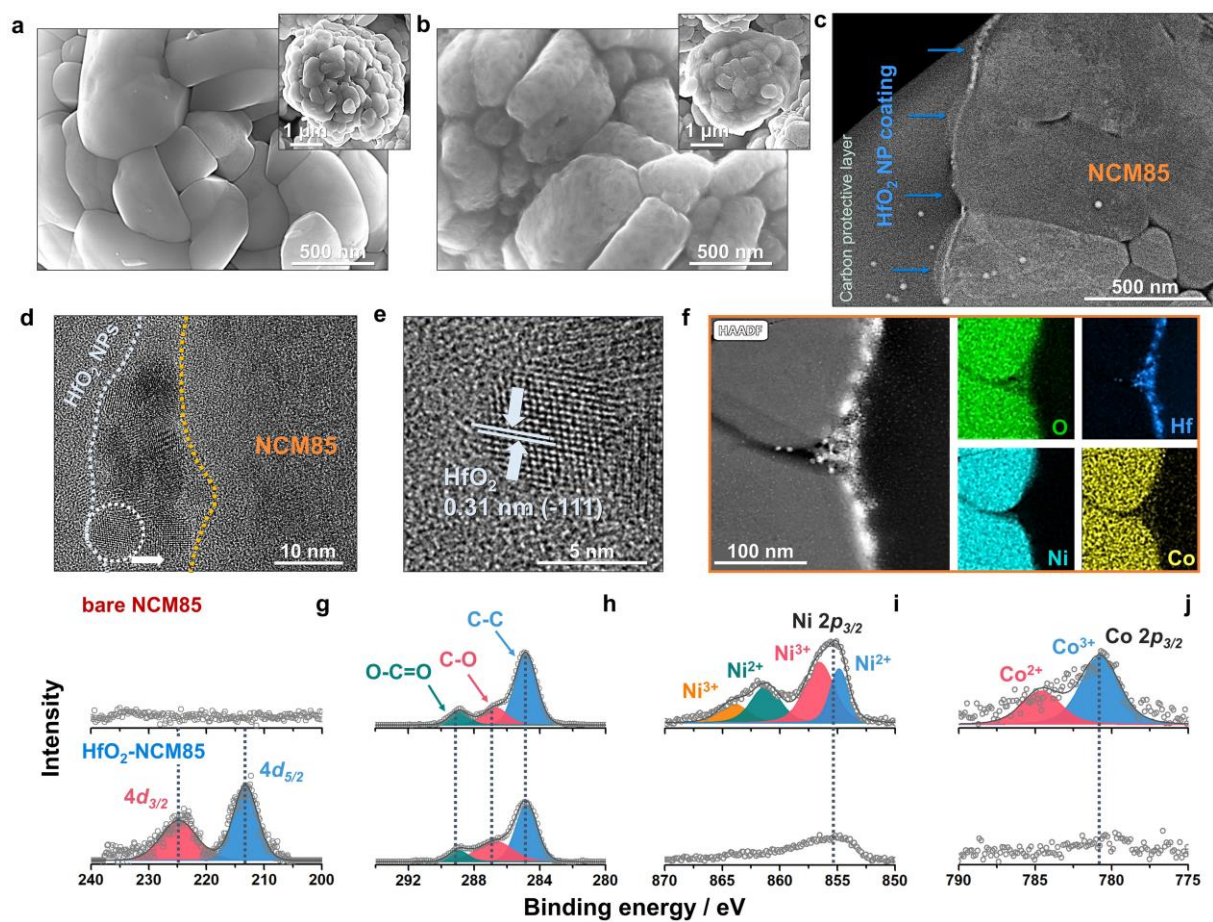


Figure 2. SEM images at different magnifications of the (a) bare NCM85 and (b) HfO_2 -NCM85 particles. (c) HAADF STEM and (d) TEM images of FIB-prepared particle cross-sections. (e) High-resolution TEM image of the area denoted by the white circle in (d). (f) STEM EDS mapping results. (g) Hf 4d, (h) C 1s, (i) Ni 2p, and (j) Co 2p XPS detail spectra for bare NCM85 (top) and HfO_2 -NCM85 (bottom). Note that the C 1s, Ni 2p, and Co 2p spectra have the same y-axis scaling for both CAMs.

The electrochemical behavior of the HfO_2 -NCM85 CAM was tested in thiophosphate-based, (pelletized) pellet-stack SSB cells and compared with bare NCM85, which served as a reference material. Both samples were mixed with $\text{Li}_6\text{PS}_5\text{Cl}$ SE and Super C65 carbon black additive for the preparation of cathode composite in powder form. The cathodes employed had a relatively high areal loading of $(11.0 \pm 0.3) \text{ mg}_{\text{NCM85}}/\text{cm}^2$, corresponding to $\sim 2 \text{ mAh}/\text{cm}^2$. The anodes in this setup were produced from LTO, Super C65, and $\text{Li}_6\text{PS}_5\text{Cl}$. All cells were tested at 45°C in the voltage range 1.35-2.75 V vs. $\text{Li}_4\text{Ti}_5\text{O}_{12}/\text{Li}_7\text{Ti}_5\text{O}_{12}$ (~ 2.9 -4.3 V vs. Li^+/Li).

The voltage profiles for the first two cycles at 0.1C rate in **Figure 3a** indicate major improvements in cyclability after coating. The performance parameters for the initial cycle are compared in the radar plot in **Figure 3b**. For HfO₂-NCM85, the specific discharge capacity and Coulomb efficiency reached high values of 203 mAh/g and 90 %, respectively. In contrast, bare NCM85 only delivered 175 mAh/g, with a much lower first-cycle Coulomb efficiency of 79 %. HfO₂-NCM85 also showed a smaller voltage drop (**Figure S7**) and higher mean voltage (**Figure 3b**) compared with bare NCM85. This suggests that the NP coating is capable of somewhat suppressing side reactions occurring at the CAM|SE interface, thus effectively reducing resistance buildup upon cycling.^{2,34} The second-cycle voltage profiles confirmed this trend. In particular, a large overpotential was evident for bare NCM85 at the beginning of the charge cycle and HfO₂-NCM85 showed virtually no capacity decay, indicating good reversibility.

For rate and long-term performance testing, the cells were charged and discharged at different C-rates of 0.1C, 0.2C, 0.5C, and 1.0C over the first 8 cycles, followed by cycling at 0.2C (**Figure 3c**). As expected, HfO₂-NCM85 showed much improved cyclability. For example, ~65% of the specific capacity was retained at 1.0C rate (relative to that at 0.1C in the initial cycle), compared to less than 40 % for bare NCM85, and the capacity retention after 200 cycles was ~70 % (135 mAh/g), compared to ~58 % (81 mAh/g) for bare NCM85 (with reference to q_{dis} at 0.2C in the 9th cycle). From the data, it can be seen that bare NCM85 showed minor capacity fading between the 9th and 60th cycle (lower overall degree of de-/lithiation), with accelerated degradation thereafter (mechanical contact loss etc.). This kind of cycling behavior has also been observed by other groups when using polycrystalline CAMs.³⁵

More detailed rate capability testing was done on the cells from 0.2C to 5.0C (**Figure 3d**). Because the NP coating exerted a positive effect on the cathode stability, HfO₂-NCM85 showed a satisfactory performance. In particular, stable specific discharge capacities of >60, 40, and 20 mAh/g were achieved at rates of 3.0C, 4.0C, and 5.0C, respectively. In contrast, bare NCM85 delivered <10 mAh/g at $\geq 3.0C$. Comparing the voltage profiles of the bare and coated NCM85-based cells, we found that the protective coating lowers the increase in overpotential with increasing C-rate (**Figure S8**). Considering the negligible (ionic/electronic) conductivity of HfO₂, it could be expected that lithium transport across the CAM|SE interface is negatively

affected after coating. However, the above results rather suggest that interfacial side reactions are responsible for the performance degradation (sluggish kinetics).²⁰ Galvanostatic intermittent titration technique (GITT) analysis (**Figure S9**) further confirmed this by demonstrating more severe polarization for bare NCM85 than HfO₂-NCM85.

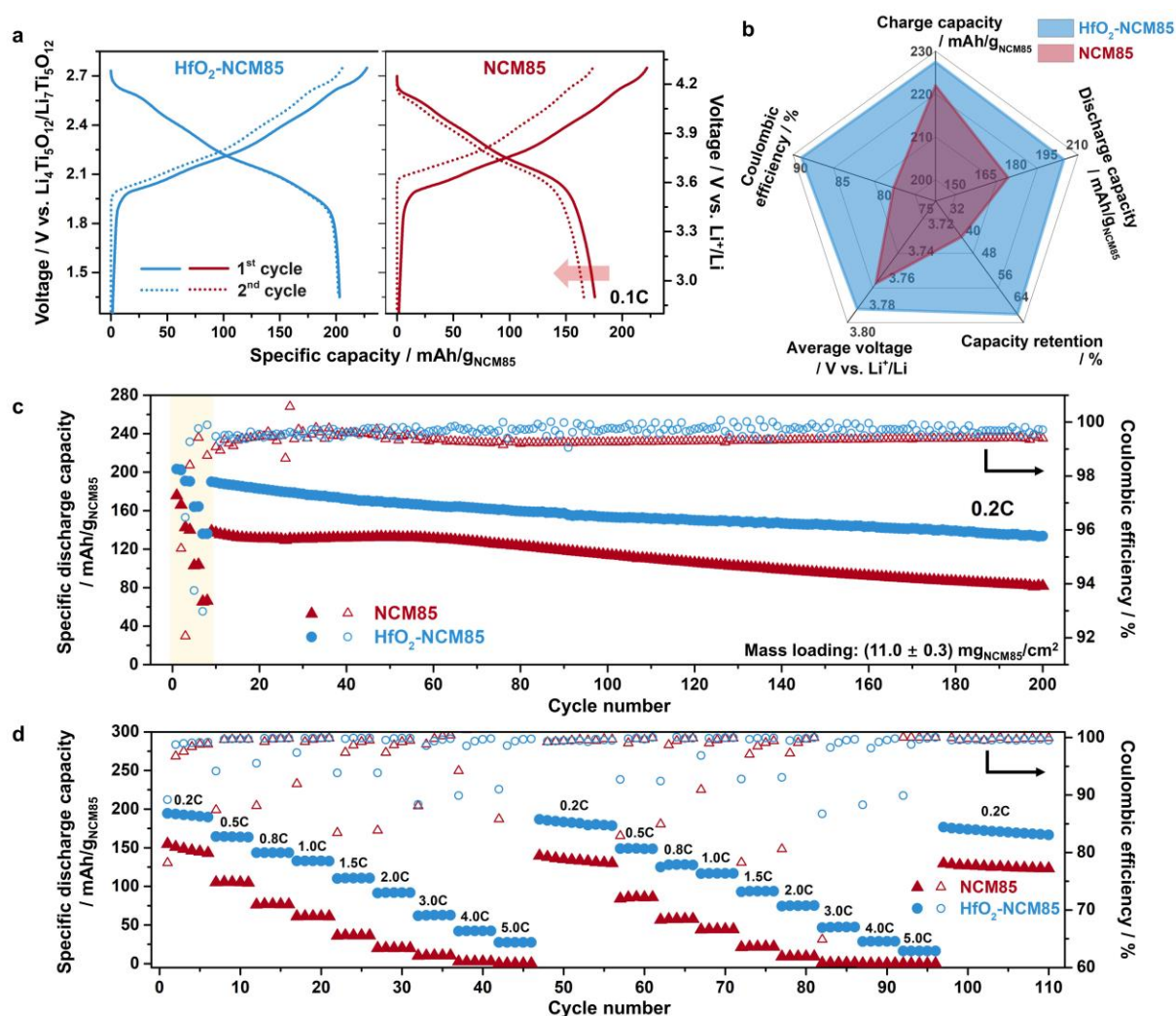


Figure 3. Cycling performance of the bare NCM85 and HfO₂-NCM85 CAMs in pellet-stack SSB cells at 45 °C. (a) Voltage profiles for the first two cycles at 0.1C rate and (b) first-cycle performance parameters. The capacity retention was calculated by dividing the discharge capacity at 1.0C by the initial discharge capacity at 0.1C. (c) Rate capability from 0.1C to 1.0C during the first 8 cycles (highlighted by the shaded area) and long-term cycling performance at 0.2C. (d) Specific discharge capacities (and Coulomb efficiencies) for various C-rates versus the cycle number.

In contrast to HfO₂-NCM85, for bare NCM85, the major capacity decay occurred in the initial cycles. To better understand the working principle of the NP coating, a series of *operando* and *ex situ* measurements were conducted on the cathodes. In general, interfacial stability problems and (chemo)mechanical degradation have been identified as two of the root causes of capacity fading and cell failure.^{36,37} Mechanical degradation (particle fracture, contact loss, etc.) primarily results from the anisotropic volume variation in NCM-type materials.^{38,39} An elegant way to probe the state of charge (SOC) of SSB cells and learn about the mechanical behavior is via monitoring the structural evolution of the CAM during cycling.⁴⁰ To this end, *operando* XRD measurements were performed using liquid-electrolyte-based coin cells containing the NCM85 and a Li metal anode (**Figures S10** and **S11**). This allows the changes in structural parameters to be directly correlated with the lithium content in the CAM [$x(\text{Li})$]. The data were then used as a reference and compared with results from *ex situ* XRD measurements conducted on the SSB cathodes in the pristine state, and after the first charge and discharge (**Figure S12** and **Table S4**). The evolution trends with Li extraction and re-intercalation are depicted in **Figures 4a** and **b**. During charge (delithiation), the lattice parameter a decreased steadily, due to Ni oxidation, leading to continuous contraction of the ab -plane.⁴⁰ In contrast, the c -axis revealed a different behavior, namely an initial gradual increase because of increasing electrostatic repulsion between the oxygen layers, followed by a strong decrease for $x(\text{Li}) \leq 0.3$ (see also **Figure S11**).^{40,41} The latter is caused by a collapse of the layered structure.^{42,43} The cell volume also decreased considerably upon achieving high degrees of delithiation, which typically impairs the cycling stability.⁴³⁻⁴⁵ XRD analysis revealed a more pronounced volume shrinkage for HfO₂-NCM85 ($\Delta V/V \approx -4.4\%$ vs. -2.8% for bare NCM85 at ~ 4.3 V vs. Li⁺/Li). This result suggests that the anisotropic volume variation has no profound effect on the initial cycling performance, especially the first-cycle reversible capacity. We believe that the small particle size of NCM85 ($d_{50} \approx 4$ μm) allows for intimate physical contact with the SE in the cathode, thereby mitigating mechanical degradation. Similar observations have been made previously for LiNiO₂.⁴⁰

Using this approach, both the reversible and irreversible capacity contributions can be determined from the Li content.⁴⁰ The specific charge capacities were calculated to be 222 and

205 mAh/g for HfO₂-NCM85 and bare NCM85, respectively, based on the cell parameters determined from *ex situ* XRD. Both values are lower than the measured capacities (227 mAh/g for HfO₂-NCM85 and 222 mAh/g for bare NCM85). Thus, the “additional” charge capacity can be attributed to the oxidative degradation of the Li₆PS₅Cl SE (among others), deteriorating the reversibility of the cell.^{2,46} A significantly larger irreversible capacity was observed for the bare NCM85, again indicating that the NP coating is capable of suppressing to some degree adverse side reactions. Note that the as-formed interphase negatively affects the charge-transport properties, thus leading to inferior capacities.

Electrochemical impedance spectroscopy (EIS) measurements conducted after the first charge confirmed this conclusion (**Figures 4c** and **d** and **Table S5**). The CAM|SE interfacial resistance ($R_{\text{CAM|SE}}$) for bare NCM85 was three times larger than that for HfO₂-NCM85. Both the bulk resistance (R_{Bulk}) and SE grain boundary resistance (R_{GB}) were similar for the different cells. The overall trend in $R_{\text{CAM|SE}}$ matched the results from the electrochemical testing.

The first-cycle specific discharge capacities were also calculated, amounting to 202 and 173 mAh/g for HfO₂-NCM85 and bare NCM85, respectively, in good agreement with the electrochemically measured ones (**Figures 4a** and **b**). This corroborates the effectiveness of the approach in determining the SOC of SSBs and further suggests that SE degradation is most pronounced during the course of the initial charge.

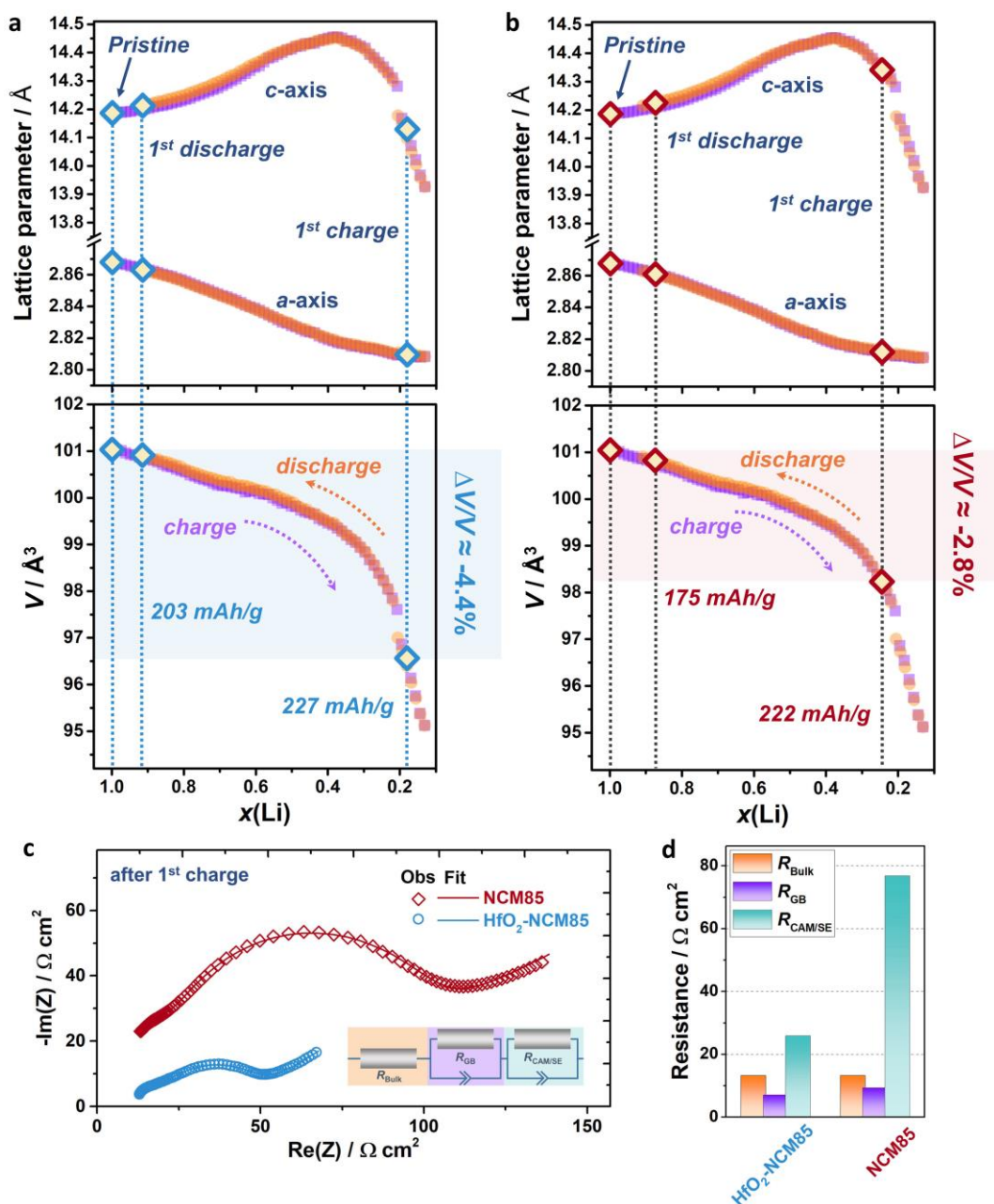


Figure 4. (a, b) Changes in lattice parameters (top) and cell volume (bottom) as a function of $x(\text{Li})$ from Rietveld refinement of *operando* XRD data obtained on a liquid-electrolyte-based Li|NCM85 reference cell, and structural evolution of (a) $\text{HfO}_2\text{-NCM85}$ and (b) bare NCM85 in pellet-stack SSB cells during the initial cycle at 0.1C rate and 45 °C from *ex situ* XRD. Note that the $x(\text{Li})$ was calculated from the electrochemical data. Refined lattice parameters and cell volume (see also **Figure S12** and **Table S4**) are denoted by blue and red diamond symbols. Measured specific capacities are also indicated. (c) Nyquist plots of the electrochemical impedance of SSB cells with $\text{HfO}_2\text{-NCM85}$ (blue) and bare NCM85 (red) after the initial charge. The inset shows the equivalent circuit used for fitting. (d) Summary of the impedance results.

The gassing behavior of the bare and coated NCM85-based SSB cells was probed using differential electrochemical mass spectrometry (DEMS). In recent years, it has been shown that certain coating chemistries can help to suppress the formation of gaseous degradation products.^{8,28} For both CAMs, four different gases were detected in the first two cycles, namely H₂, O₂, CO₂, and SO₂ (**Figures 5** and **S13**). Among these, the formation and release of O₂ and SO₂ are of importance in the discussion of side reactions occurring at the CAM|SE interface.⁸ In general, oxygen in a reactive state has been demonstrated to be released at high SOC, e.g. $\geq 80\%$ for NCM811 (80 % Ni), due to destabilization of the crystal lattice.^{47,48} The requirement of 80 % SOC was not realized for bare NCM85 (**Figures 5a**). While cells using the latter CAM achieved an SOC closer to 75 % (~206 mAh/g) in the initial cycle, those with HfO₂-NCM85 revealed an SOC of about 83 % (~229 mAh/g). However, because of cathode inhomogeneities, O₂ release may even occur below 80 %. For thiophosphate-based SSBs, side reactions of the SE with O₂ have been reported, with the formation of SO₂ as a gaseous product (clear indication of SE decomposition).^{49,50} Thus, correlated O₂ and SO₂ evolution should be observed, which was indeed the case for bare NCM85, where sharp $m/z = 32$ and 64 signals were detected around 4.2 V vs. Li⁺/Li (**Figures 5b** and **c**). In contrast, no O₂ and/or SO₂ gas evolved in the HfO₂-NCM85-based cells. A possible explanation for this result is that the coating inhibits the release of lattice oxygen. Recently, Guo *et al.* have shown that oleic acid-induced surface engineering leads to (spinel/layered) heterostructure formation, which apparently strengthened the surface by preventing the layered to spinel/rocksalt phase transformation.⁵¹ Given that oleic acid was used in the HfO₂ NP dispersion, the possibility of a similar effect cannot be excluded. The data presented provide profound evidence that the coating helps to stabilize cathode interfaces, which has a positive effect on the cell cyclability (less capacity fading despite more severe volume variation).

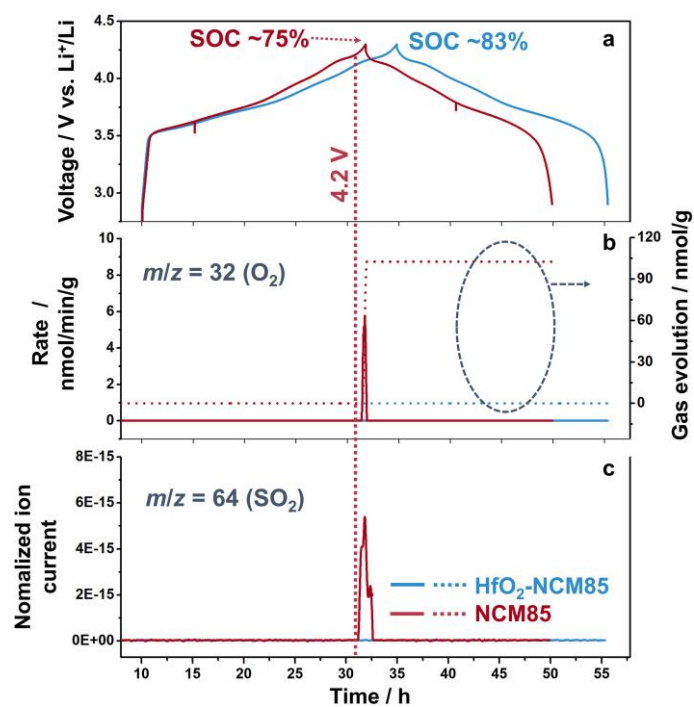


Figure 5. *In situ* gas analysis of SSB cells with bare NCM85 (red) and HfO₂-NCM85 (blue). (a) First-cycle voltage profiles at 0.05C rate and 45 °C, (b) time-resolved evolution rates (left y-axis) and cumulative amounts (right y-axis) of O₂, and (c) normalized ion currents for SO₂.

Apart from the first-cycle characteristics and rate capability, there were also major differences in the long-term cycling performance between the bare and coated NCM85 CAMs. To better understand these, EIS measurements were conducted on the cells after 60 and 200 cycles at 0.2C rate and 45 °C (**Figure S14** and **Table S5**). The cathode interfacial resistance grew upon cycling in both cases. For bare NCM85, the $R_{CAM/SE}$ increased by a factor of ~10 relative to the initial (charge) cycle and was ~4.5 times larger than that for HfO₂-NCM85. This means that side reactions occurred continuously at the interfaces with the SE during cycling, but much more pronounced in the case of bare NCM85.

Next, FIB-prepared samples were probed using cross-sectional SEM for visualizing the microstructural evolution. As shown in **Figures 6a** and **b**, the structure/morphology of HfO₂-NCM85 (after 60 cycles) was well preserved; the degree of particle fracture was very low. By contrast, SEM and HAADF STEM imaging (**Figures 6c-e**) revealed cracking of the bare NCM85 secondary particles, leading to the formation of reactive surfaces and inducing unwanted side reactions, as confirmed by EDS mapping of Cl and P (**Figure 6e**).²⁸ These results

are consistent with the trends seen from electrochemical testing and EIS analysis. Several studies have attributed intergranular CAM cracking in LIBs to the anisotropic volume variation during cycling.^{52,53} However, as demonstrated by XRD, the absolute change in cell volume of HfO₂-NCM85 was larger than that for bare NCM85 as a result of the larger capacity delivered. Thus, it seems likely that the particle fracture might be rather related to the (electro)chemical side reactions occurring at the CAMISE interface. A recent report by Han *et al.* supports this hypothesis.⁵⁴ The protective coating somewhat suppressed unfavorable side reactions, thereby ensuring particle integrity and longevity.

This was further corroborated by *ex situ* studies combining STEM with electron energy-loss spectroscopy (EELS). The O K-edge spectrum for bare NCM85 (**Figures 6f** and **g**) showed a gradual fading of the pre-edge feature from the bulk toward the surface, indicating the presence of vacancies in the O sublattice and transition-metal reduction.⁵⁵ The latter was also evident from the Ni L-edge spectrum in **Figure 6g** (decrease in intensity of the shoulder peak at ~856 eV).⁵⁶ In contrast, much weaker signs of O-defect formation and Ni reduction were found for HfO₂-NCM85 (**Figures 6h** and **i**). This suggests that the surface degradation of NCM85 is closely connected to the interfacial side reactions.⁵⁴ The NP coating mitigated this effect and preserved high surface coverage after cycling, as demonstrated by STEM and EDS (**Figure 6j**).²⁸

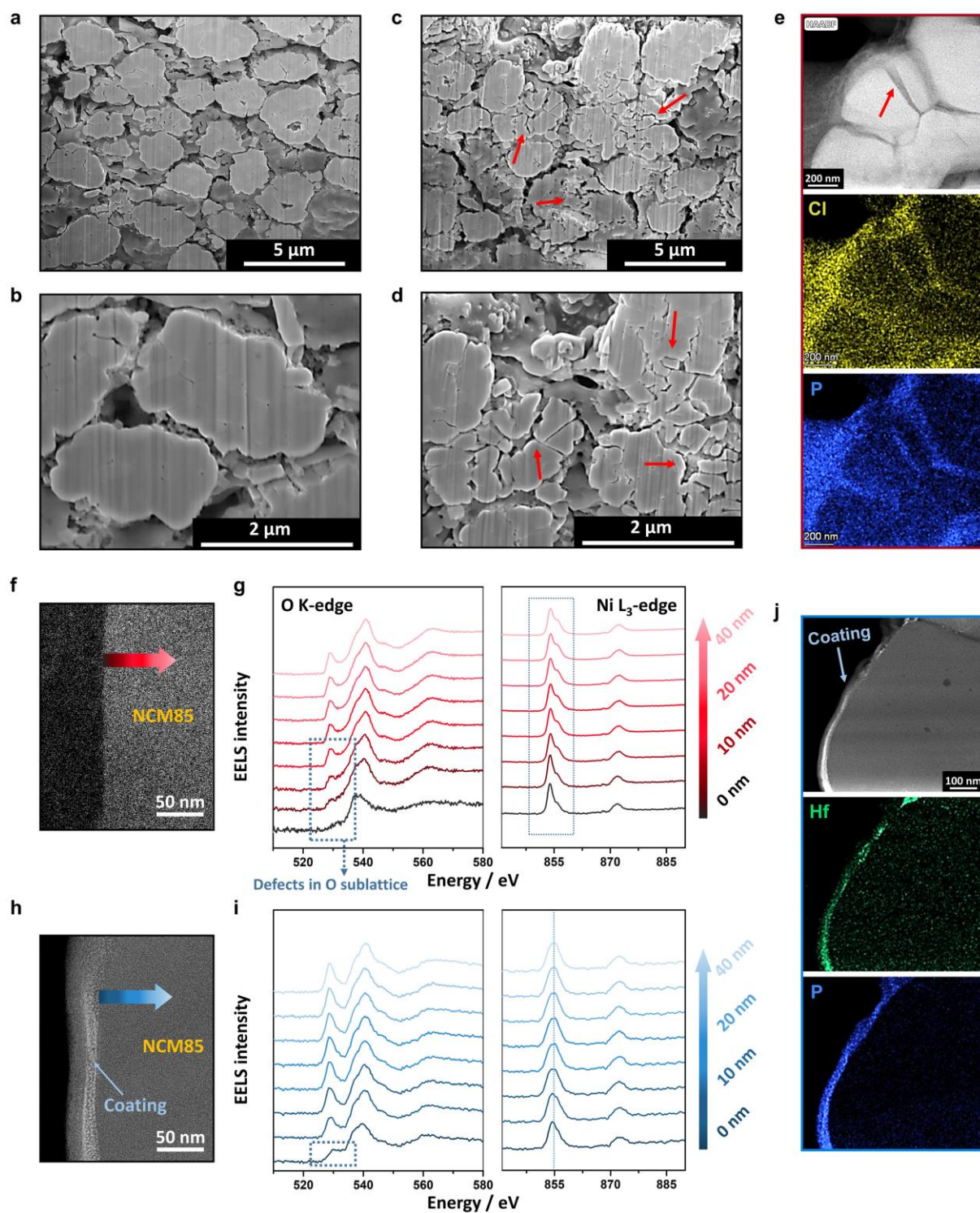


Figure 6. CAM degradation after SSB cell cycling at 0.2C rate and 45 °C (60 cycles) probed by SEM and HAADF STEM including EELS and EDS. Cross-sectional SEM images at different magnifications of the cathodes with (a, b) HfO₂-NCM85 and (c, d) bare NCM85. EDS mapping results for (e) bare NCM85 and (j) HfO₂-NCM85. HAADF STEM images and EELS line scans from the surface inwards to the bulk for (f, g) bare NCM85 and (h, i) HfO₂-NCM85.

Intergranular cracking is indicated by red arrows in (c-e) and the coating by blue arrows in (h) and (j).

XPS was used to identify the chemical nature of the degradation products formed at the interfaces with the SE. In the following, we limit the discussion to the S 2p and P 2p core-level regions (**Figure 7a**), which revealed the most significant changes. The S 2p (reference) detail spectrum collected from the pristine $\text{Li}_6\text{PS}_5\text{Cl}$ SE showed three doublet peaks. The main peak at 161.4 eV (S 2p_{3/2}) could be assigned to PS_4^{3-} . The minor one at the lower binding energy side (160.0 eV) is probably due to the free S^{2-} in the argyrodite structure (or Li_2S), while that at 163.3 eV indicated the presence of a small amount of polysulfides.^{40,57,58} The P 2p detail spectrum contained two doublet peaks, due to the PS_4^{3-} units (P 2p_{3/2} peak at 131.9 eV) and some impurity species ($\text{P}_2\text{S}_6^{2-}$, Li_3PO_4 , etc., with the P 2p_{3/2} peak at 132.8 eV).^{46,59} The intensity of the polysulfide peaks in the S 2p spectrum was increased for the bare NCM85 and HfO_2 -NCM85 cathodes after cycling (60 cycles). At the same time, new doublet peaks appeared at binding energies beyond 166.0 eV, suggesting the formation of oxygenated sulfur (SO_x) compounds.^{38,58,60} The latter can be directly attributed to the side reactions occurring at the CAM|SE interface (note that the NCM85 CAM was the only oxygen source present in the positive electrode of the cells).⁸ As expected, lower intensities of the respective peaks (lower relative amounts) were observed for HfO_2 -NCM85 (**Figure S15**), confirming the above results. A similar trend was also seen in the P 2p data, with the appearance of a new doublet peak (P 2p_{3/2} peak at 134.1 eV) resulting from the formation of metal phosphates and/or metaphosphates (i.e. oxygenated phosphorus (PO_x) compounds due to CAM|SE side reactions).^{8,60} This is in agreement with the interdiffusion observed by STEM EDS (**Figure S16**). Overall, the interfacial degradation leads to buildup of a resistive passivation layer containing, among others, SO_x and PO_x species, thereby impeding charge transfer and transport.^{8,28,54}

The pristine (**Figures 7b** and **S17**) and cycled cathodes (**Figures 7c** and **d**) were also imaged using SEM. As can be seen from the data, the CAM secondary particles were well embedded in the SE matrix (indicated by arrows in the respective images). In the pristine state (prior to cycling), there were no visible differences between the cathodes using the bare NCM85 or

HfO₂-NCM85. However, for bare NCM85, SE degradation (indicated by arrows) was very evident from the change in electrode morphology after cycling (200 cycles). In the case of HfO₂-NCM85, the cathode largely maintained its initial appearance, further emphasizing the robustness of the CAM|SE interface. Notably, void formation and contact loss on the micrometer level were not observed, neither for HfO₂-NCM85 nor for bare NCM85. This agrees with the XRD results, indicating that mechanical effects, due to volume changes of the CAM particles, play a minor role in the capacity-fading behavior.

Taken together, the findings collectively demonstrate that the side reactions at the CAM|SE interface not only cause the formation of a passivation layer and loss of active material, but also negatively affect the integrity of the NCM85 particle structure. These problems were mitigated, to a large extent, by coating the CAM free surface with HfO₂ NPs, leading to considerable improvements in cycling performance.

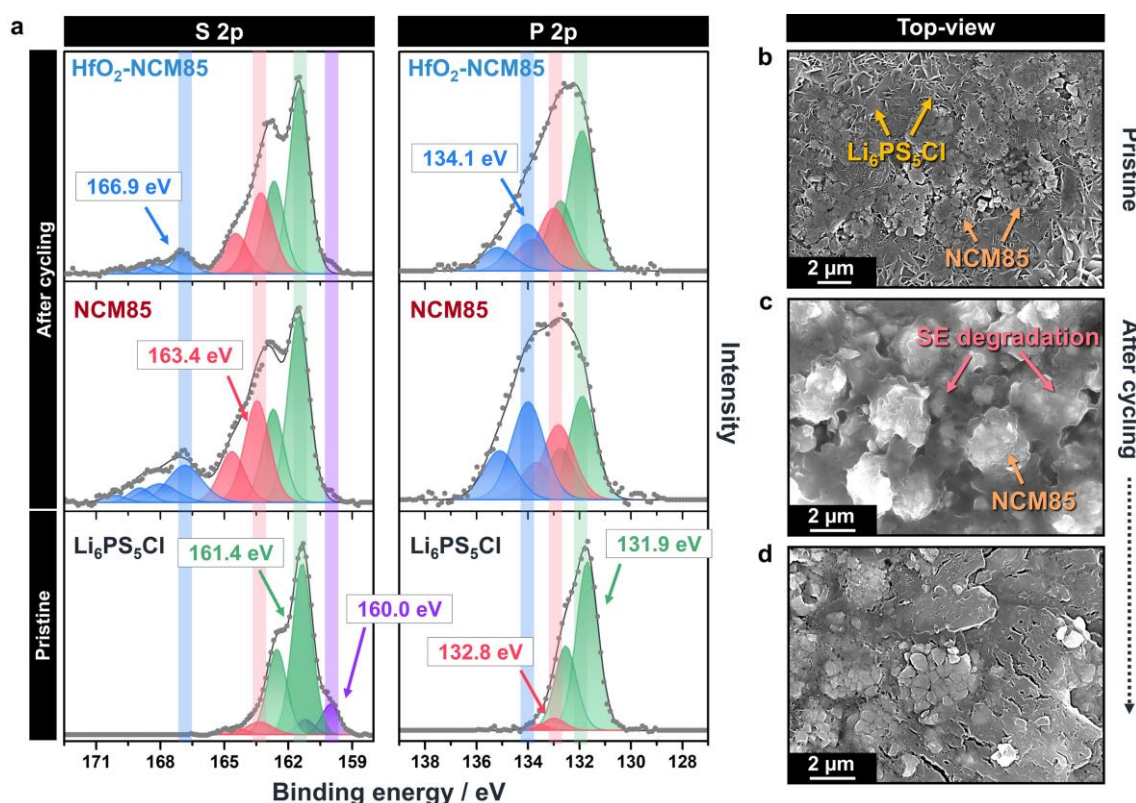


Figure 7. (a) XPS detail spectra of the S 2p (left) and P 2p (right) regions for pristine Li₆PS₅Cl and cathodes using bare NCM85 and HfO₂-NCM85 after SSB cell cycling (60 cycles at 0.2C rate and 45 °C). Top-view SEM images of cathodes with (b, d) HfO₂-NCM85 and (c) bare NCM85 taken (b) prior to and (c, d) after cycling (200 cycles).

The effectiveness of the coating in liquid-electrolyte-based LIB cells was studied too. To this end, high-loading cathodes ($11.3 \pm 0.3 \text{ mg}_{\text{NCM85}}/\text{cm}^2$) were tested in the voltage range of 2.9-4.3 V vs. Li^+/Li in coin half-cells. The first-cycle voltage profiles at 0.2C rate and 45 °C and corresponding differential capacity curves are shown in **Figures S18** and **S19**, suggesting similar electrochemical behavior for the bare NCM85 and $\text{HfO}_2\text{-NCM85}$, with specific discharge capacities of 209 and 206 mAh/g and Coulomb efficiencies of 93.8 and 93.6 %, respectively. **Figure 8a** presents a performance comparison of both CAMs in pellet-stack SSB and conventional LIB cells. The solid-state environment resulted in a lower Coulomb efficiency in the initial cycle and some drop in capacity due to interfacial stability problems.^{37,40} Upon applying the NP coating to the NCM85, the capacity retention, relative to the corresponding LIB cells, improved from 74 % for bare NCM85 to 95 % for $\text{HfO}_2\text{-NCM85}$. $\text{HfO}_2\text{-NCM85}$ also showed better long-term cycling in LIBs, with 70 vs. 61 % capacity retention after 200 cycles at 0.2C rate and 25 °C (**Figure 8b**).

Slurry-cast electrodes were also prepared and incorporated into SSBs to learn about the adaptability of $\text{HfO}_2\text{-NCM85}$ to wet processing.⁴⁹ The slurry-cast cathodes tested in this work had an areal loading of $16.4 \text{ mg}_{\text{NCM85}}/\text{cm}^2$, with a similar composition to the pelletized counterparts, but using glassy $1.5\text{Li}_2\text{S}\text{-}0.5\text{P}_2\text{S}_5\text{-LiI}$ as SE and 1 wt. % polyisobutylene binder. The cycling behavior of slurry-cast and pelletized (binder-free) cathodes with $1.5\text{Li}_2\text{S}\text{-}0.5\text{P}_2\text{S}_5\text{-LiI}$ and $\text{Li}_6\text{PS}_5\text{Cl}$, respectively, in cells at 0.2C rate and 45 °C is shown in **Figure 8c**. Using the slurry-cast cathode in the SSB setup, high area-specific capacities ($\sim 2.3 \text{ mAh}/\text{cm}^2$) were achieved in the initial cycles and also a much better capacity retention of 94 % after 200 cycles, compared to 83 % after 60 cycles for the dry-processed (binder-free) cathode. This improvement could be linked to (i) enhanced contact between cathode and SE, (ii) higher uniformity of the slurry-cast cathode, and (iii) the fact that the Young's modulus of glassy SEs is typically beneficial for mitigating mechanical degradation.^{49,61}

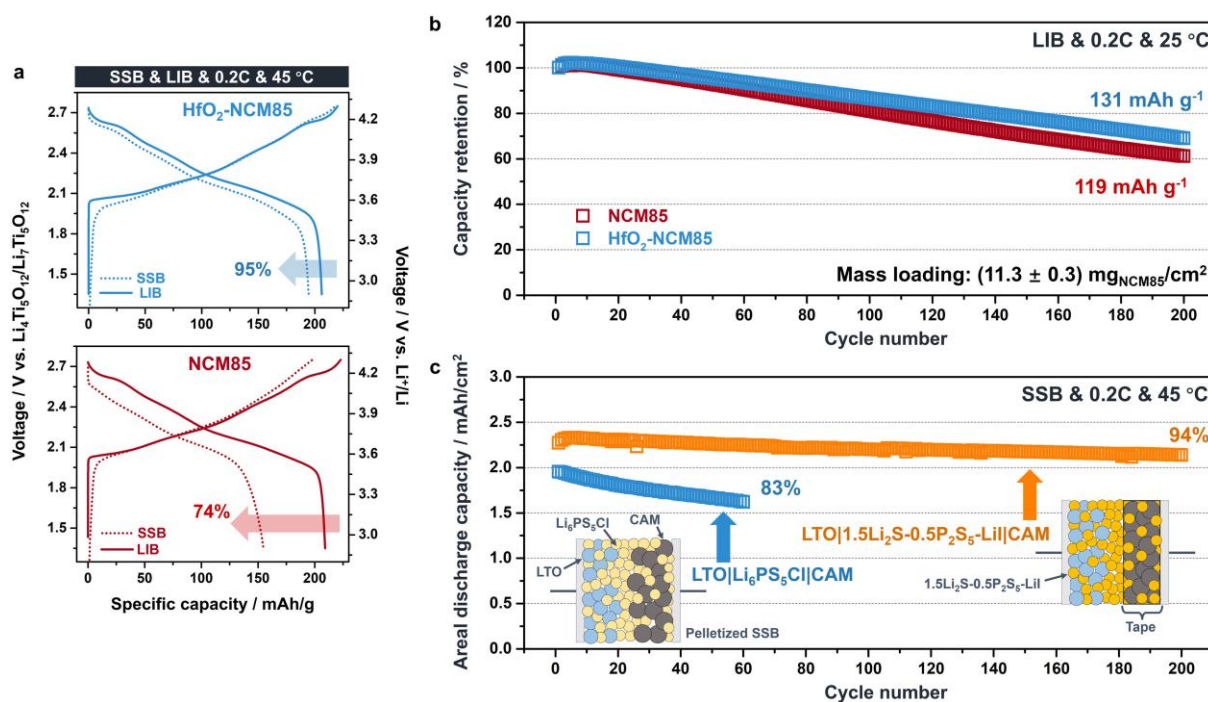


Figure 8. (a) Initial voltage profiles of pelletized SSB and LIB cells using cathodes with HfO₂-NCM85 (top) and bare NCM85 (bottom). (b) Long-term cycling performance of LIB cells. (c) Cyclability of slurry-cast (with 1.5Li₂S-0.5P₂S₅-LiI SE) and pelletized (with Li₆PS₅Cl SE) SSB cathodes with HfO₂-NCM85.

CONCLUSIONS

A homogeneously distributed secondary particle coating on a Ni-rich NCM cathode material and its benefits to the electrochemical performance has been presented. Surface stabilization using an appropriate solvent mitigated issues with particle agglomeration and allowed for the uniform deposition of individual nanoparticles on the CAM surface. Electrochemical testing showed that the coated material exhibits improvements in specific capacity, capacity retention, and Coulomb efficiency compared with its uncoated counterpart when employed in thiophosphate-based SSBs. Complementary characterization conducted on the positive electrodes prior to, during, and after cycling indicated that the protective coating not only suppresses interfacial side reactions, but also inhibits particle fracture and outgassing, thereby improving the stability of the cathode structure/morphology and CAM|SE interface. The coated material was also tested in high-loading, slurry-cast cathodes with a glassy 1.5Li₂S-0.5P₂S₅-LiI solid electrolyte and found to maintain stable, long-term cycling at 45 °C. Compatibility with

wet processing of electrodes is essential for the practical application of inorganic solid-state batteries. The nanoparticle coating also improved the cycling stability of the Ni-rich NCM cathode in conventional liquid-electrolyte-based Li-ion cells. While the results presented are encouraging, we believe that the overall performance can be increased further by using this generic surface-modification strategy and tailoring the coating chemistry.

EXPERIMENTAL SECTION

Preparation of HfO₂ Nanoparticles and CAM Coating. The solvothermal synthesis of HfO₂ nanoparticles and their surface functionalization using oleic acid and oleylamine are detailed elsewhere.^{24,25} Quasi-transparent chloroform-based nanoparticle dispersions having a solid content of ~20 mg/mL were achieved in this work. The HfO₂ nanoparticles were then applied as coating material to the NCM85 CAM (BASF SE) following a procedure reported previously.⁸ Prior to coating, the as-received CAM was heated at 750 °C in oxygen flow to eliminate surface impurities (residual Li). Depending on the solid content, a certain volume of nanoparticle dispersion was added to 2 g NCM85 in a beaker. Finally, chloroform was added to achieve 20 mL total volume and the beaker was sealed using Parafilm. Next, the suspension was agitated by ultrasonication for 15 min, thereby enabling uniform mixing of the HfO₂ nanoparticles and the NCM85 secondary particles. Afterwards, the Parafilm was removed and the suspension was placed in an oil bath at 60 °C with continuous stirring until the chloroform was evaporated. The resulting black powder was collected and treated at ambient temperature in a vacuum overnight, followed by heating at 400 °C in oxygen flow for 2 h. After natural cooling, the coated NCM85 CAM was transferred to an Ar glovebox for further processing.

Electrode Preparation. The composites used for the preparation of pelletized and slurry-cast electrodes were prepared as reported elsewhere.^{8,49} Two types of SEs were used in this work, argyrodite Li₆PS₅Cl (NEI Corp.) and glassy 1.5Li₂S-0.5P₂S₅-LiI. For the latter material, stoichiometric amounts of precursors (LiI, 99.99 %, Alfa Aesar; P₂S₅, 99 %, Sigma-Aldrich; Li₂S, 99.9 %, Sigma-Aldrich) were mixed in a 70 mL zirconia jar under Ar atmosphere. The sealed jar was then transferred to a planetary ball mill (FRITSCH) and the powder mixture milled at 450 rpm for 12 h.⁶¹ The as-prepared SE was used as separator, as well as in the cathode

and anode of tape-cast SSBs. For the cathode composite, CAM, SE ($\text{Li}_6\text{PS}_5\text{Cl}$ for pelletized cells and glassy $1.5\text{Li}_2\text{S}-0.5\text{P}_2\text{S}_5-\text{LiI}$ for tape-cast cells), and Super C65 carbon additive (TIMCAL Ltd.) were mixed in a weight ratio of 69.3:29.7:1.0. For the anode composite, the weight ratio of carbon-coated LTO (NEI Corp.), SE to Super C65 was set to 30:60:10. Slurry-cast electrodes were prepared from the glassy SE-based cathode composite described above. The latter was first pre-wetted with anhydrous *o*-xylene (97 %, Sigma-Aldrich) and mixed at 600 rpm for 2 min using a centrifugal planetary mixer. The solid content in the slurry was set to 64 wt. %. Next, polyisobutylene binder (Oppanol N 150, BASF SE) solution was added dropwise to achieve a CAM:SE:Super C65:binder weight ratio of 68.6:29.4:1.0:1.0. After further mixing at 2000 rpm for 6 min, the as-obtained slurry was cast onto Al foil under Ar atmosphere using a mini tape casting coater from MTI Corp. The different mixing steps and casting conditions are described in more detail elsewhere.^{49,61} The slurry-cast cathode tape was first dried in the glovebox at room temperature and ambient pressure for 4 h and then subjected to further drying in a vacuum for 12 h. For the testing in LIBs, the CAM was incorporated into an *N*-methyl-2-pyrrolidone slurry with Super C65 and polyvinylidene difluoride binder in a weight ratio of 94:3:3 using a centrifugal planetary mixer. The slurry was cast onto Al foil at a thickness of 140 μm and dried at 120 °C in a vacuum. Finally, the electrode was calendered at 15 N/mm and cut into circular electrodes of diameter 13 mm. The areal loading was $\sim 11.3 \text{ mg}_{\text{NCM85}}/\text{cm}^2$.

Cell assembly. A customized setup was used for the pelletized SSBs, containing stainless steel dies as current collectors and a 10 mm diameter PEEK ring.⁸ First, about 100 mg SE was compacted at 62.5 MPa. Then, 65-66 mg anode composite and 12-13 mg cathode composite were placed on either side of the SE pellet. 440 MPa pressure was applied to the assembled cell to ensure intimate contact between the different components. For the tape-cast SSBs, a 9 mm diameter cathode was punched out and then placed onto the compacted glassy SE separator layer. The amounts of SE separator and anode were the same as for the pelletized cells described above. During galvanostatic cycling, an external pressure of 81 MPa was maintained. 2032 coin cells were used to probe the cycling performance of LIBs. Lithium metal served as counter electrode (Albemarle Germany GmbH). The separator (GF/D from Whatman) soaked with 95

μL of LP57 (1 M LiPF_6 in 3:7 by weight ethylene carbonate (EC):ethyl methyl carbonate (EMC), BASF SE) was placed between working and counter electrode.

Electrochemical Measurements. Both the cell cyclability and rate performance were tested at 25 °C and 45 °C, with 1C corresponding to 190 mA/g_{NCM85}, using a MACCOR battery cycler. The voltage range was set to 1.35-2.75 V vs. $\text{Li}_4\text{Ti}_5\text{O}_{12}/\text{Li}_7\text{Ti}_5\text{O}_{12}$ (about 2.9-4.3 V vs. Li^+/Li) and 2.9-4.3 V vs. Li^+/Li for the SSBs and LIBs, respectively. EIS was conducted on the SSB cells at 45 °C (7 mV voltage amplitude, 7 MHz to 100 mHz frequency change) using an SP-300 multichannel potentiostat (Bio-Logic). GITT measurements were also performed at 45 °C on the MACCOR battery cycler. After the initial cycle, the cells were given 30 min constant charge or discharge current pulses at 0.05C, with a 4 h relaxation period between each pulse.

Characterization. SEM imaging was done using a Zeiss Leo 1530 microscope equipped with a field emission source. TEM measurements (HRTEM, SAED, STEM EDS, and EELS) were conducted at an accelerating voltage of 300 kV using a double-corrected Themis-Z microscope (Thermo Fisher Scientific) equipped with a HAADF STEM detector, a Super-X EDX detector, and a Gatan Continuum 970 HighRes image filter. The STEM EDS maps were acquired at a beam current of 200 pA. Sample cross-sections were prepared using a dual-beam focused Ga ion beam (FIB) in an FEI Strata 400 at 30 kV. Carbon layers were deposited by ion beam-induced deposition to protect the surface coating. The thinned samples were further cleaned at 5 kV/2 kV. ICP-OES measurements were carried out using an iCAP 7600 Duo (Thermo Fischer Scientific) and a PerkinElmer Optima 4300 DV. ATR-IR spectra were collected from 1800 to 600 cm^{-1} using an ALPHA FT-IR spectrometer (Bruker). XRD data were acquired using a STOE Stadi-P diffractometer with a DECTRIS MYTHEN 1K strip detector in Debye-Scherrer geometry ($\lambda = 1.5406 \text{ \AA}$). The instrumental contribution to the peak broadening was obtained by measuring a NIST 640f Si standard reference material as line broadening reference. Rietveld refinement was performed using GSAS-II.⁶² For refinement of NCM structural models against the diffraction data, the scale factor, zero shift, and size/strain broadening parameters were allowed to vary. A fixed background was fitted to the data using a Chebyshev polynomial function with 13 terms. In the structural model, the unit cell parameters, the oxygen z-coordinate, and the atomic displacement parameters (isotropic) for each site were refined. Atoms occupying

the same site were constrained to have the same atomic parameters, and site occupancy factors were constrained such that each site remained fully occupied. XPS measurements were carried out on a SPECS XPS system with a PHOIBOS 150 energy analyzer using monochromatic Al K α radiation ($\lambda = 1486.6$ eV), a take-off angle of 45°, and pass energies of 30 and 90 eV for detail and survey scans, respectively. The C1s peak (adventitious carbon) at 284.8 eV was used for binding energy calibration. Peak fitting was done with the CasaXPS software assuming Shirley-type backgrounds and mixed Gaussian-Lorentzian peak shapes. For peak doublets in the P 2p and S 2p core-level regions, the intensity ratio (2:1) and spin-orbit splitting (0.84 eV for P 2p, 1.18 eV for S 2p) were set to the expected values.⁶³ The DEMS setup used for *in situ* gas analysis is described in detail elsewhere.^{8,49} In this case, galvanostatic cycling was done at a rate of 0.05C and 45 °C in the voltage range of 2.3-3.7 V vs. In/InLi (about 2.9-4.3 V vs. Li⁺/Li) using a VMP3 multichannel potentiostat, with a 10 h OCV period prior to testing.

ASSOCIATED CONTENT

Supporting Information

Characterization of the HfO₂ NPs; XRD analysis of the CAMs and microscopy results; voltage profiles of SSB cells and GITT data; results from *operando* and *ex situ* XRD; additional DEMS and XPS data; Nyquist plots of the electrochemical impedance and fitting results; post mortem STEM EDS analysis; voltage profiles of LIB cells and differential capacity plots; ICP-OES results; refined structural parameters; and characteristics of NP coatings in the battery field. The supporting information is available free of charge on the ACS publication website.

AUTHOR INFORMATION

Corresponding Authors

*E-mail: yuan.ma@kit.edu (Y. Ma)

*E-mail: yushu.tang@kit.edu (Y. Tang)

*E-mail: torsten.brezesinski@kit.edu (T. Brezesinski)

Author Contributions

‡Y. Ma and R. Zhang contributed equally to this work.

Notes

The authors declare no competing financial interest.

ACKNOWLEDGMENT

This study was supported by BASF SE. The authors further acknowledge the support from the Karlsruhe Nano Micro Facility (KNMFi, www.knmf.kit.edu), a Helmholtz research infrastructure at Karlsruhe Institute of Technology (KIT, www.kit.edu). The authors thank Dr. Thomas Bergfeldt (KIT) for collecting ICP-OES data. Y.T. acknowledges financial support from the German Research Foundation (DFG) under project ID 390874152 (POLiS Cluster of Excellence).

REFERENCES

- (1) Janek, J.; Zeier, W. G. A Solid Future for Battery Development. *Nat. Energy* **2016**, *1*, 16141.
- (2) Banerjee, A.; Wang, X.; Fang, C.; Wu, E. A.; Meng, Y. S. Interfaces and Interphases in All-Solid-State Batteries with Inorganic Solid Electrolytes. *Chem. Rev.* **2020**, *120*, 6878–6933.
- (3) Chen, R.; Li, Q.; Yu, X.; Chen, L.; Li, H. Approaching Practically Accessible Solid-State Batteries: Stability Issues Related to Solid Electrolytes and Interfaces. *Chem. Rev.* **2020**, *120*, 6820–6877.
- (4) Zhou, L.; Kwok, C. Y.; Shyamsunder, A.; Zhang, Q.; Wu, X.; Nazar, L. F. A New Halospinel Superionic Conductor for High-Voltage All Solid State Lithium Batteries. *Energy Environ. Sci.* **2020**, *13*, 2056–2063.
- (5) Lee, Y.-G.; Fujiki, S.; Jung, C.; Suzuki, N.; Yashiro, N.; Omoda, R.; Ko, D.-S.; Shiratsuchi, T.; Sugimoto, T.; Ryu, S.; Ku, J. H.; Watanabe, T.; Park, Y.; Aihara, Y.; Im, D.; Han, I. T. High-Energy Long-Cycling All-Solid-State Lithium Metal Batteries Enabled by Silver–Carbon Composite Anodes. *Nat. Energy* **2020**, *5*, 299–308.
- (6) Xu, K. Electrolytes and Interphases in Li-Ion Batteries and Beyond. *Chem. Rev.* **2014**, *114*, 11503–11618.

- (7) Park, K. H.; Bai, Q.; Kim, D. H.; Oh, D. Y.; Zhu, Y.; Mo, Y.; Jung, Y. S. Design Strategies, Practical Considerations, and New Solution Processes of Sulfide Solid Electrolytes for All-Solid-State Batteries. *Adv. Energy Mater.* **2018**, *8*, 1800035.
- (8) Ma, Y.; Teo, J. H.; Walther, F.; Ma, Y.; Zhang, R.; Mazilkin, A.; Tang, Y.; Goonetilleke, D.; Janek, J.; Bianchini, M.; Brezesinski, T. Advanced Nanoparticle Coatings for Stabilizing Layered Ni-Rich Oxide Cathodes in Solid-State Batteries. *Adv. Funct. Mater.* **2022**, *32*, 2111829.
- (9) Richards, W. D.; Miara, L. J.; Wang, Y.; Kim, J. C.; Ceder, G. Interface Stability in Solid-State Batteries. *Chem. Mater.* **2016**, *28*, 266–273.
- (10) Culver, S. P.; Koerver, R.; Zeier, W. G.; Janek, J. On the Functionality of Coatings for Cathode Active Materials in Thiophosphate-Based All-Solid-State Batteries. *Adv. Energy Mater.* **2019**, *9*, 1900626.
- (11) Tan, D. H. S.; Banerjee, A.; Chen, Z.; Meng, Y. S. From Nanoscale Interface Characterization to Sustainable Energy Storage Using All-Solid-State Batteries. *Nat. Nanotechnol.* **2020**, *15*, 170–180.
- (12) Zhu, Y.; He, X.; Mo, Y. Origin of Outstanding Stability in the Lithium Solid Electrolyte Materials: Insights from Thermodynamic Analyses Based on First-Principles Calculations. *ACS Appl. Mater. Interfaces* **2015**, *7*, 23685–23693.
- (13) Xiao, Y.; Miara, L. J.; Wang, Y.; Ceder, G. Computational Screening of Cathode Coatings for Solid-State Batteries. *Joule* **2019**, *3*, 1252–1275.
- (14) Nisar, U.; Muralidharan, N.; Essehli, R.; Amin, R.; Belharouak, I. Valuation of Surface Coatings in High-Energy Density Lithium-Ion Battery Cathode Materials. *Energy Storage Mater.* **2021**, *38*, 309–328.
- (15) Jung, S. H.; Oh, K.; Nam, Y. J.; Oh, D. Y.; Br uner, P.; Kang, K.; Jung, Y. S. Li_3BO_3 – Li_2CO_3 : Rationally Designed Buffering Phase for Sulfide All-Solid-State Li-Ion Batteries. *Chem. Mater.* **2018**, *30*, 8190–8200.
- (16) Ohta, N.; Takada, K.; Sakaguchi, I.; Zhang, L.; Ma, R.; Fukuda, K.; Osada, M.; Sasaki, T. LiNbO_3 -Coated LiCoO_2 as Cathode Material for All Solid-State Lithium Secondary Batteries. *Electrochem. Commun.* **2007**, *9*, 1486–1490.

- (17) Negi, R. S.; Culver, S. P.; Mazilkin, A.; Brezesinski, T.; Elm, M. T. Enhancing the Electrochemical Performance of $\text{LiNi}_{0.70}\text{Co}_{0.15}\text{Mn}_{0.15}\text{O}_2$ Cathodes Using a Practical Solution-Based Al_2O_3 Coating. *ACS Appl. Mater. Interfaces* **2020**, *12*, 31392–31400.
- (18) Ito, S.; Fujiki, S.; Yamada, T.; Aihara, Y.; Park, Y.; Kim, T. Y.; Baek, S.-W.; Lee, J.-M.; Doo, S.; Machida, N. A Rocking Chair Type All-Solid-State Lithium Ion Battery Adopting $\text{Li}_2\text{O}-\text{ZrO}_2$ Coated $\text{LiNi}_{0.8}\text{Co}_{0.15}\text{Al}_{0.05}\text{O}_2$ and a Sulfide Based Electrolyte. *J. Power Sources* **2014**, *248*, 943–950.
- (19) Ahmed, B.; Xia, C.; Alshareef, H. N. Electrode Surface Engineering by Atomic Layer Deposition: A Promising Pathway toward Better Energy Storage. *Nano Today* **2016**, *11*, 250–271.
- (20) Kitsche, D.; Tang, Y.; Ma, Y.; Goonetilleke, D.; Sann, J.; Walther, F.; Bianchini, M.; Janek, J.; Brezesinski, T. High Performance All-Solid-State Batteries with a Ni-Rich NCM Cathode Coated by Atomic Layer Deposition and Lithium Thiophosphate Solid Electrolyte. *ACS Appl. Energy Mater.* **2021**, *4*, 7338–7345.
- (21) Cho, J.; Kim, Y.-W.; Kim, B.; Lee, J.-G.; Park, B. A Breakthrough in the Safety of Lithium Secondary Batteries by Coating the Cathode Material with AlPO_4 Nanoparticles. *Angew. Chem. Int. Ed.* **2003**, *42*, 1618–1621.
- (22) Lee, Y.-S.; Shin, W.-K.; Kannan, A. G.; Koo, S. M.; Kim, D.-W. Improvement of the Cycling Performance and Thermal Stability of Lithium-Ion Cells by Double-Layer Coating of Cathode Materials with Al_2O_3 Nanoparticles and Conductive Polymer. *ACS Appl. Mater. Interfaces* **2015**, *7*, 13944–13951.
- (23) Geng, C.; Liu, A.; Dahn, J. R. Impact of Aluminum Added to Ni-Based Positive Electrode Materials by Dry Particle Fusion. *Chem. Mater.* **2020**, *32*, 6097–6104.
- (24) De Roo, J.; Van den Broeck, F.; De Keukeleere, K.; Martins, J. C.; Van Driessche, I.; Hens, Z. Unravelling the Surface Chemistry of Metal Oxide Nanocrystals, the Role of Acids and Bases. *J. Am. Chem. Soc.* **2014**, *136*, 9650–9657.
- (25) Buha, J.; Arçon, D.; Niederberger, M.; Djerdj, I. Solvothermal and Surfactant-Free Synthesis of Crystalline Nb_2O_5 , Ta_2O_5 , HfO_2 , and Co-Doped HfO_2 Nanoparticles. *Phys. Chem. Chem. Phys.* **2010**, *12*, 15537–15543.

- (26) Jun, Y.-w.; Choi, J.-s.; Cheon, J. Shape Control of Semiconductor and Metal Oxide Nanocrystals through Nonhydrolytic Colloidal Routes. *Angew. Chem. Int. Ed.* **2006**, *45*, 3414–3439.
- (27) Garnweitner, G.; Goldenberg, L. M.; Sakhno, O. V.; Antonietti, M.; Niederberger, M.; Stumpe, J. Large-Scale Synthesis of Organophilic Zirconia Nanoparticles and Their Application in Organic–Inorganic Nanocomposites for Efficient Volume Holography. *Small* **2007**, *3*, 1626–1632.
- (28) Yoon, M.; Dong, Y.; Hwang, J.; Sung, J.; Cha, H.; Ahn, K.; Huang, Y.; Kang, S. J.; Li, J.; Cho, J. Reactive Boride Infusion Stabilizes Ni-Rich Cathodes for Lithium-Ion Batteries. *Nat. Energy* **2021**, *6*, 362–371.
- (29) Barreca, D.; Milanov, A.; Fischer, R. A.; Devi, A.; Tondello, E. Hafnium Oxide Thin Film Grown by ALD: An XPS Study. *Surf. Sci. Spectra* **2007**, *14*, 34–40.
- (30) Liu, C.-F.; Tang, X.-G.; Guo, X.-B.; Liu, Q.-X.; Jiang, Y.-P.; Tang, Z.-H.; Li, W.-H. Photodiode Characteristics of HfO₂ Thin Films Prepared by Magnetron Sputtering. *Mater. Des.* **2020**, *188*, 108465.
- (31) Ma, Y.; Ma, Y.; Kim, G.-T.; Diemant, T.; Behm, R. J.; Geiger, D.; Kaiser, U.; Varzi, A.; Passerini, S. Superior Lithium Storage Capacity of α -MnS Nanoparticles Embedded in S-Doped Carbonaceous Mesoporous Frameworks. *Adv. Energy Mater.* **2019**, *9*, 1902077.
- (32) Qi, X.; Blizanac, B.; DuPasquier, A.; Lal, A.; Niehoff, P.; Placke, T.; Oljaca, M.; Li, J.; Winter, M. Influence of Thermal Treated Carbon Black Conductive Additive on the Performance of High Voltage Spinel Cr-Doped LiNi_{0.5}Mn_{1.5}O₄ Composite Cathode Electrode. *J. Electrochem. Soc.* **2015**, *162*, A339–A343.
- (33) Dou, X.; Hasa, I.; Hekmatfar, M.; Diemant, T.; Behm, R. J.; Buchholz, D.; Passerini, S. Pectin, Hemicellulose, or Lignin? Impact of the Biowaste Source on the Performance of Hard Carbons for Sodium-Ion Batteries. *ChemSusChem* **2017**, *10*, 2668–2676.
- (34) Wang, C.; Liang, J.; Zhao, Y.; Zheng, M.; Li, X.; Sun, X. All-Solid-State Lithium Batteries Enabled by Sulfide Electrolytes: From Fundamental Research to Practical Engineering Design. *Energy Environ. Sci.* **2021**, *14*, 2577–2619.
- (35) Shi, T.; Zhang, Y.-Q.; Tu, Q.; Wang, Y.; Scott, M. C.; Ceder, G. Characterization of

- Mechanical Degradation in an All-Solid-State Battery Cathode. *J. Mater. Chem. A* **2020**, *8*, 17399–17404.
- (36) Famprikis, T.; Canepa, P.; Dawson, J. A.; Islam, M. S.; Masquelier, C. Fundamentals of Inorganic Solid-State Electrolytes for Batteries. *Nat. Mater.* **2019**, *18*, 1278–1291.
- (37) Koerver, R.; Aygün, I.; Leichtweiß, T.; Dietrich, C.; Zhang, W.; Binder, J. O.; Hartmann, P.; Zeier, W. G.; Janek, J. Capacity Fade in Solid-State Batteries: Interphase Formation and Chemomechanical Processes in Nickel-Rich Layered Oxide Cathodes and Lithium Thiophosphate Solid Electrolytes. *Chem. Mater.* **2017**, *29*, 5574–5582.
- (38) Jung, S. H.; Kim, U.-H.; Kim, J.-H.; Jun, S.; Yoon, C. S.; Jung, Y. S.; Sun, Y.-K. Ni-Rich Layered Cathode Materials with Electrochemo-Mechanically Compliant Microstructures for All-Solid-State Li Batteries. *Adv. Energy Mater.* **2020**, *10*, 1903360.
- (39) Liu, X.; Zheng, B.; Zhao, J.; Zhao, W.; Liang, Z.; Su, Y.; Xie, C.; Zhou, K.; Xiang, Y.; Zhu, J.; Wang, H.; Zhong, G.; Gong, Z.; Huang, J.; Yang, Y. Electrochemo-Mechanical Effects on Structural Integrity of Ni-Rich Cathodes with Different Microstructures in All Solid-State Batteries. *Adv. Energy Mater.* **2021**, *11*, 2003583.
- (40) Ma, Y.; Teo, J. H.; Kitsche, D.; Diemant, T.; Strauss, F.; Ma, Y.; Goonetilleke, D.; Janek, J.; Bianchini, M.; Brezesinski, T. Cycling Performance and Limitations of LiNiO₂ in Solid-State Batteries. *ACS Energy Lett.* **2021**, *6*, 3020–3028.
- (41) Van der Ven, A.; Aydinol, M. K.; Ceder, G.; Kresse, G.; Hafner, J. First-Principles Investigation of Phase Stability in Li_xCoO₂. *Phys. Rev. B* **1998**, *58*, 2975–2987.
- (42) Li, W.; Asl, H. Y.; Xie, Q.; Manthiram, A. Collapse of LiNi_{1-x-y}Co_xMn_yO₂ Lattice at Deep Charge Irrespective of Nickel Content in Lithium-Ion Batteries. *J. Am. Chem. Soc.* **2019**, *141*, 5097–5101.
- (43) Li, H.; Zhang, N.; Li, J.; Dahn, J. R. Updating the Structure and Electrochemistry of Li_xNiO₂ for 0 ≤ x ≤ 1. *J. Electrochem. Soc.* **2018**, *165*, A2985–A2993.
- (44) Li, H.; Liu, A.; Zhang, N.; Wang, Y.; Yin, S.; Wu, H.; Dahn, J. R. An Unavoidable Challenge for Ni-Rich Positive Electrode Materials for Lithium-Ion Batteries. *Chem. Mater.* **2019**, *31*, 7574–7583.
- (45) Goonetilleke, D.; Sharma, N.; Pang, W. K.; Peterson, V. K.; Petibon, R.; Li, J.; Dahn, J.

- R. Structural Evolution and High-Voltage Structural Stability of $\text{Li}(\text{Ni}_x\text{Mn}_y\text{Co}_z)\text{O}_2$ Electrodes. *Chem. Mater.* **2019**, *31*, 376–386.
- (46) Walther, F.; Randau, S.; Schneider, Y.; Sann, J.; Rohnke, M.; Richter, F. H.; Zeier, W. G.; Janek, J. Influence of Carbon Additives on the Decomposition Pathways in Cathodes of Lithium Thiophosphate-Based All-Solid-State Batteries. *Chem. Mater.* **2020**, *32*, 6123–6136.
- (47) Jung, R.; Metzger, M.; Maglia, F.; Stinner, C.; Gasteiger, H. A. Oxygen Release and Its Effect on the Cycling Stability of $\text{LiNi}_x\text{Mn}_y\text{Co}_z\text{O}_2$ (NMC) Cathode Materials for Li-Ion Batteries. *J. Electrochem. Soc.* **2017**, *164*, A1361–A1377.
- (48) Jung, R.; Strobl, P.; Maglia, F.; Stinner, C.; Gasteiger, H. A. Temperature Dependence of Oxygen Release from $\text{LiNi}_{0.6}\text{Mn}_{0.2}\text{Co}_{0.2}\text{O}_2$ (NMC622) Cathode Materials for Li-Ion Batteries. *J. Electrochem. Soc.* **2018**, *165*, A2869–A2879.
- (49) Teo, J. H.; Strauss, F.; Tripković, Đ.; Schweidler, S.; Ma, Y.; Bianchini, M.; Janek, J.; Brezesinski, T. Design-of-Experiments-Guided Optimization of Slurry-Cast Cathodes for Solid-State Batteries. *Cell Rep. Phys. Sci.* **2021**, *2*, 100465.
- (50) Mahne, N.; Renfrew, S. E.; McCloskey, B. D.; Freunberger, S. A. Electrochemical Oxidation of Lithium Carbonate Generates Singlet Oxygen. *Angew. Chem. Int. Ed.* **2018**, *57*, 5529–5533.
- (51) Guo, W.; Zhang, C.; Zhang, Y.; Lin, L.; He, W.; Xie, Q.; Sa, B.; Wang, L.; Peng, D.-L. A Universal Strategy toward the Precise Regulation of Initial Coulombic Efficiency of Li-Rich Mn-Based Cathode Materials. *Adv. Mater.* **2021**, *33*, 2103173.
- (52) Miller, D. J.; Proff, C.; Wen, J. G.; Abraham, D. P.; Bareño, J. Observation of Microstructural Evolution in Li Battery Cathode Oxide Particles by In Situ Electron Microscopy. *Adv. Energy Mater.* **2013**, *3*, 1098–1103.
- (53) Yu, H.; Cao, Y.; Chen, L.; Hu, Y.; Duan, X.; Dai, S.; Li, C.; Jiang, H. Surface Enrichment and Diffusion Enabling Gradient-Doping and Coating of Ni-Rich Cathode toward Li-Ion Batteries. *Nat. Commun.* **2021**, *12*, 4564.
- (54) Han, Y.; Jung, S. H.; Kwak, H.; Jun, S.; Kwak, H. H.; Lee, J. H.; Hong, S.-T.; Jung, Y. S. Single- or Poly-Crystalline Ni-Rich Layered Cathode, Sulfide or Halide Solid Electrolyte:

- Which Will Be the Winners for All-Solid-State Batteries? *Adv. Energy Mater.* **2021**, *11*, 2100126.
- (55) Lin, F.; Nordlund, D.; Markus, I. M.; Weng, T.-C.; Xin, H. L.; Doeff, M. M. Profiling the Nanoscale Gradient in Stoichiometric Layered Cathode Particles for Lithium-Ion Batteries. *Energy Environ. Sci.* **2014**, *7*, 3077–3085.
- (56) Yoon, W.-S.; Balasubramanian, M.; Chung, K. Y.; Yang, X.-Q.; McBreen, J.; Grey, C. P.; Fischer, D. A. Investigation of the Charge Compensation Mechanism on the Electrochemically Li-Ion Deintercalated $\text{Li}_{1-x}\text{Co}_{1/3}\text{Ni}_{1/3}\text{Mn}_{1/3}\text{O}_2$ Electrode System by Combination of Soft and Hard X-Ray Absorption Spectroscopy. *J. Am. Chem. Soc.* **2005**, *127*, 17479–17487.
- (57) Wang, L.; Sun, X.; Ma, J.; Chen, B.; Li, C.; Li, J.; Chang, L.; Yu, X.; Chan, T.-S.; Hu, Z.; Noked, M.; Cui, G. Bidirectionally Compatible Buffering Layer Enables Highly Stable and Conductive Interface for 4.5 V Sulfide-Based All-Solid-State Lithium Batteries. *Adv. Energy Mater.* **2021**, *11*, 2100881.
- (58) Park, S. W.; Oh, G.; Park, J.-W.; Ha, Y.-C.; Lee, S.-M.; Yoon, S. Y.; Kim, B. G. Graphitic Hollow Nanocarbon as a Promising Conducting Agent for Solid-State Lithium Batteries. *Small* **2019**, *15*, 1900235.
- (59) Wang, B.; Liu, J.; Sun, Q.; Li, R.; Sham, T.-K.; Sun, X. Atomic Layer Deposition of Lithium Phosphates as Solid-State Electrolytes for All-Solid-State Microbatteries. *Nanotechnology* **2014**, *25*, 504007.
- (60) Auvergniot, J.; Cassel, A.; Ledeuil, J.-B.; Viallet, V.; Seznec, V.; Dedryvère, R. Interface Stability of Argyrodite $\text{Li}_6\text{PS}_5\text{Cl}$ toward LiCoO_2 , $\text{LiNi}_{1/3}\text{Co}_{1/3}\text{Mn}_{1/3}\text{O}_2$, and LiMn_2O_4 in Bulk All-Solid-State Batteries. *Chem. Mater.* **2017**, *29*, 3883–3890.
- (61) Teo, J. H.; Strauss, F.; Walther, F.; Ma, Y.; Payandeh, S.; Scherer, T.; Bianchini, M.; Janek, J.; Brezesinski, T. The Interplay between (Electro)Chemical and (Chemo)Mechanical Effects in the Cycling Performance of Thiophosphate-Based Solid-State Batteries. *Mater. Futures* **2022**, *1*, 015102.
- (62) Toby, B. H.; Von Dreele, R. B. *GSAS-II*: The Genesis of a Modern Open-Source All Purpose Crystallography Software Package. *J. Appl. Crystallogr.* **2013**, *46*, 544–549.

- (63) Moulder, J. F.; Stickle, W. J.; Sobol, P. E.; Bomben, K. D. *Handbook of X-Ray Photoelectron Spectroscopy: A Reference Book of Standard Spectra for Identification and Interpretation of XPS Data*, Physical Electronics: Eden Prairie.; Perkin-Elmer: US-MN, 1995.

TOC Graphics

